Appl. Phys. B (2015) 120:711–721
DOI 10.1007/s00340-015-6187-9

Applied Physics B
Lasers and Optics

Spatial hole burning in Yb:YAG thin-disk lasers

Christian Vorholt[1] · **Ulrich Wittrock**[1]

Received: 15 April 2015 / Accepted: 21 July 2015 / Published online: 31 July 2015

Abstract The spatially varying intensity in a standing wave resonator leads to spatial hole burning in the gain medium of a laser. The spatial hole burning changes the gain of different longitudinal modes and can thus determine the optical spectrum of the laser. We simulate this longitudinal mode competition in standing wave resonators of thin-disk lasers. The resulting optical spectra of the laser are compared to measured optical spectra. We examine two types of resonators: I-resonators and V-resonators with different angles of incidence. In V-resonators, the non-normal incidence of the laser beam on the disk lifts the degeneracy of the polarization. Experiments show that the slight gain advantage for the *p*-polarization does not lead to polarized emission. For both types of resonators, the measured spectra are in good agreement with the simulated ones. The simulations allow to study the influence of spectral intracavity losses on the optical spectrum of a thin-disk laser.

1 Introduction

In an Yb:YAG thin-disk laser that is pumped considerably above the threshold, usually two or more longitudinal modes can be observed in the optical spectrum. Experiments have shown that the modes are regularly spaced in wavelength, with a typical spacing of 1 nm [1]. Thus, it is many hundred times larger than the resonator's free spectral range. The large spacing of the modes makes it easier to force the laser to oscillate at a single frequency by using intra-cavity spectrally selective elements. In this paper, we show that the spacing of the modes is caused by spatial hole burning. The large mode spacing occurs because an Yb:YAG thin-disk laser is an extreme case of a gain-at-the-end laser [2, 3].

Recently, we demonstrated an intra-cavity pumped thin-disk laser with a very low quantum defect of 1.7 % [4]. The laser consists of a diode-pumped thin-disk laser whose output coupler is replaced by another Yb:YAG disk. The absorption of the disk inside the resonator represents a wavelength-dependent loss for the diode-pumped laser. Hence, the diode-pumped laser avoids wavelengths that experience high losses. A dichroic mirror was used to limit the maximum oscillating wavelength of the diode-pumped laser. Measurements of its optical spectrum revealed oscillation on two or more modes, just as observed in conventional thin-disk lasers. The results from this paper enable us to customize dichroic mirrors to force the diode-pumped laser to oscillate at the desired wavelength.

Braun and Kaertner reproduced the optical spectrum of a Nd : YVO_4 rod laser by using a sophisticated numerical simulation [2, 3]. Their simulation incorporates inhomogeneous gain saturation due to spatial hole burning in an I-resonator. This is a resonator with two mirrors and a straight, unfolded beam that resemble the letter "I." We performed a similar simulation for the optical spectrum of Yb:YAG thin-disk lasers with I-resonators and V-resonators. In V-resonators, the arrangement of the disk, the two mirrors, and the laser beam resembles the letter "V." A more complex two-dimensional standing wave pattern arises that alters the spacing of the observed modes. We experimentally investigate the influence of the angle of incidence on the optical spectrum of the laser and compare the results to simulations. The gain medium of our

✉ Christian Vorholt
cvorholt@fh-muenster.de

[1] Photonics Laboratory, Muenster University of Applied Sciences, Stegerwaldstraße 39, 48565 Steinfurt, Germany

thin-disk laser is a circular disk made of Yb:YAG, which has a diameter of 14 mm and a thickness of approximately 130 µm. The disk has a spherical curvature leading to a focal length of 1 m. The front side of the disk is AR coated, and the back side has an HR coating for 940 nm and for 1030 nm.

In the I-resonator, the standing waves of different frequencies each have a node at the output coupler and at the HR-coated back side of the disk. Hence, the gain close to the HR coating is unsaturated. As one moves a quarter wavelength along the resonator axis toward the output coupler, the antinodes of all standing waves add up and the gain is strongly saturated. As one moves further along the resonator axis toward the output coupler, the amplitude of the sum of all standing waves decreases, because the standing waves get out of phase. At a particular distance from the HR coating of the disk, the node of one standing wave will coincide with the antinode of another standing wave. This spatial dephasing distance ℓ_D is given by $\ell_\mathrm{D} = c_0/(4n\Delta\nu)$, where c_0 is the speed of light in vacuum, n is the refractive index of the medium, and $\Delta\nu$ is the frequency difference between two dephased standing waves. By replacing the dephasing distance with the thickness of the disk, we can calculate the frequency difference that is necessary so that the standing waves of two modes fully dephase at the AR-end of the disk. Our simulations and our experiments have shown that this is roughly the frequency difference if two longitudinal modes are present.

For comparison with measured optical spectra, we express the frequency difference as a wavelength difference with respect to an average wavelength. The wavelength difference is approximately given by $\Delta\lambda = \lambda_\mathrm{a}^2/(4dn)$, where d is the thickness of the disk and λ_a is the average wavelength in vacuum of the oscillating modes. For our disk, the wavelength difference is approximately 1.1 nm for an average wavelength of 1030 nm. Since the gain bandwidth of Yb:YAG is approximately 5.5 nm, the laser can oscillate on several of these modes [5].

2 Spatial hole burning in a V-resonator

Thin-disk lasers are usually set up with V-resonators. The folding mirror of the "V" is the HR coating on the back side of the disk. Figure 1 shows a typical setup. The waves hit the disk at an angle θ_0 with respect to the surface normal. Thus, the degeneracy of the polarization is lifted and the waves are *s*-polarized or *p*-polarized with respect to the plane of incidence. Hence, two different sets of standing wave patterns emerge: one set of *s*-polarized light and an other for *p*-polarized light.

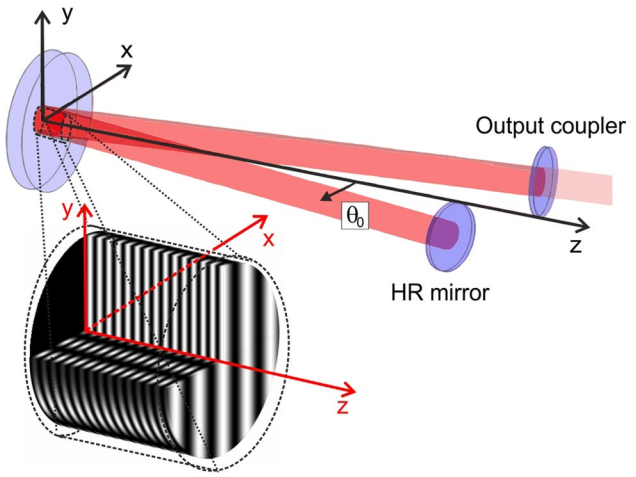

Fig. 1 V-resonator of a thin-disk laser. The coordinate system is centered at the intersection of the disk's axis with the HR coating. The *inset* shows an *s*-polarized standing wave pattern inside the disk. For better visibility, the wavelength of the standing wave pattern is exaggerated and the thickness of the disk is not to scale. *Note* the different periodicity of the pattern in the *x*-direction and in the *z*-direction

2.1 Standing wave pattern

We have calculated the phase shifts for *s*-polarization and for *p*-polarization on reflection at a typical broadband HR coating [6], using the definition of the reflection coefficient from [7]. For the *s*-polarization, the phase shift deviates by 1.8 % from π at an angle of incidence of 30°. The phase shift for the *p*-polarization deviates by 1.9 % from π. For smaller angles of incidence, the phase shift for *s*-polarization and *p*-polarization approaches π. Thus, we assume the phase shifts for *s* -polarization and *p*-polarization to be equal to π. The monochromatic plane waves inside the resonator are described by four complex electric fields. The fields are given by

$$\mathbf{E}_1(\mathbf{r},t) = [E_0^{(p)}\left(\hat{x}\cos\theta + \hat{z}\sin\theta\right) - E_0^{(s)}\hat{y}] \times \exp\left[\mathrm{i}(\omega t - \mathbf{k}_1\cdot\mathbf{r})\right] \tag{1}$$

$$\mathbf{E}_2(\mathbf{r},t) = [E_0^{(p)}\left(-\hat{x}\cos\theta + \hat{z}\sin\theta\right) + E_0^{(s)}\hat{y}] \times \exp\left[\mathrm{i}(\omega t - \mathbf{k}_2\cdot\mathbf{r})\right] \tag{2}$$

$$\mathbf{E}_3(\mathbf{r},t) = [E_0^{(p)}\left(\hat{x}\cos\theta - \hat{z}\sin\theta\right) - E_0^{(s)}\hat{y}] \times \exp\left[\mathrm{i}(\omega t + \mathbf{k}_2\cdot\mathbf{r})\right] \tag{3}$$

$$\mathbf{E}_4(\mathbf{r},t) = [E_0^{(p)}\left(-\hat{x}\cos\theta - \hat{z}\sin\theta\right) + E_0^{(s)}\hat{y}] \times \exp\left[\mathrm{i}(\omega t + \mathbf{k}_1\cdot\mathbf{r})\right], \tag{4}$$

where $\mathbf{E}_1$ is the field propagating from the HR mirror toward the HR coating of the disk, $\mathbf{E}_2$ is the field propagating from the

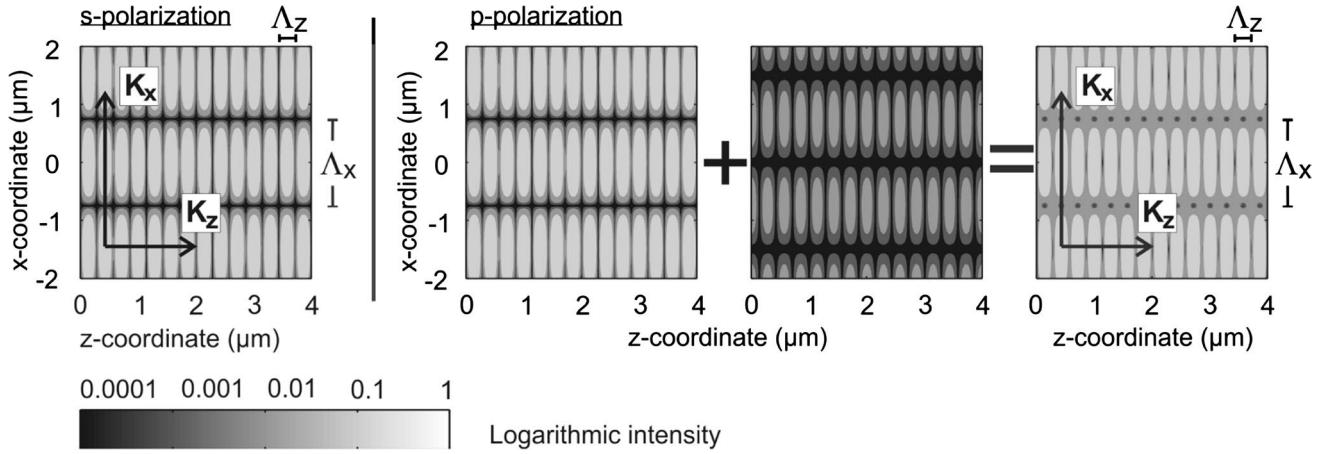

Fig. 2 For the purpose of illustration, the standing wave patterns inside the disk are shown for an angle of incidence of $\theta_0 = 20°$. In contrast to the *s*-polarized standing wave pattern, the *p*-polarized standing wave pattern is the sum of two individual standing wave patterns. The two individual standing wave patterns are spatially out of phase. The wavelength is 1030 nm. $\mathbf{K}_z$ and $\mathbf{K}_x$ are the grating vectors pointing into the *z*-direction and into the *x*-direction. Λ_z and Λ_x denote the grating periods along the *z*-axis and along the *x*-axis

HR coating of the disk toward the output coupler, $\mathbf{E}_3$ the field propagating from the output coupler toward the HR coating of the disk, and $\mathbf{E}_4$ is the field propagating from the HR coating of the disk toward the HR mirror. θ is the angle inside the disk, between the surface normal of the HR coating (*z*-axis) and the propagation direction of the wave. θ is related to the angle of incidence θ_0 via Snell's law $\theta = \sin^{-1}(1/n \sin\theta_0)$, where n is the refractive index of the disk.

The position vector $\mathbf{r}$ is given by $\mathbf{r} = (x, y, z)$. The unit vectors pointing in the x-direction, y-direction, and z-direction are denoted by $\hat{x}$, $\hat{y}$, and $\hat{z}$, respectively, see Fig. 1. ω is the angular frequency, and t is the time. The real, scalar components of the electric field that are polarized perpendicular and parallel with respect to the plane of incidence are given by $E_0^{(s)}$ and $E_0^{(p)}$, respectively. We assume that the fields

$\mathbf{E}_1, \mathbf{E}_2, ..., \mathbf{E}_4$ have constant amplitudes, because the round-trip gain and the output coupling are usually only a few percent in thin-disk lasers. The wave vectors $\mathbf{k}_1$ and $\mathbf{k}_2$ are in the plane of incidence and have angles of $\pi - \theta$ and θ with respect to the *z*-axis.

Summing up and squaring the four complex electric field vectors from Eqs. (1–4) yields the overall standing wave intensity patterns inside the disk. The *s*-polarized standing wave pattern, $I^{(s)}$, reads

$$I^{(s)}(\mathbf{r}, \theta) = 16 I_0^{(s)} \cos^2(kx \sin\theta) \sin^2(kz \cos\theta) \tag{5}$$

and the *p*-polarized standing wave pattern, $I^{(p)}$, reads

$$\begin{aligned} I^{(p)}(\mathbf{r}, \theta) = {} & 16 I_0^{(p)} \cos^2(kx \sin\theta) \sin^2(kz \cos\theta) \cos^2\theta \\ & + 16 I_0^{(p)} \sin^2(kx \sin\theta) \cos^2(kz \cos\theta) \sin^2\theta, \end{aligned} \tag{6}$$

where k is given by $k = 2\pi n/\lambda_0$, n is the refractive index of the disk, and λ_0 is the wavelength in vacuum. The variables $I_0^{(s)}$ and $I_0^{(p)}$ are the maximum intensities associated with the *s*-polarized standing wave pattern and the *p*-polarized standing wave pattern, respectively.

The *p*-polarized standing wave pattern comprises two individual standing wave patterns. The two individual standing wave patterns are associated with the first summand and the second summand in Eq. (6), respectively. Assuming equal amplitudes, the first summand is identical to the *s*-polarized standing wave pattern except for a factor of $\cos^2\theta$. Thus, for small angles of incidence, the *s* -polarized standing wave pattern and the *p*-polarized standing wave pattern are equal. When the angle of incidence becomes larger, the second summand in Eq. (6) becomes significant. The second summand yields a standing wave pattern that is spatially out of phase with respect to the *s* -polarized standing wave pattern. Thus, the *p*-polarized standing wave pattern can exploit gain that cannot be exploited by the *s*-polarized standing wave pattern. However, the gain advantage for the *p*-polarization is small, as we will show in Sect. 5.3.1. Figure 2 illustrates the *s*-polarized standing wave pattern, the two individual *p*-polarized standing wave patterns, and the resulting *p*-polarized standing wave pattern.

2.2 Grating periods

Due to the periodicity of the standing wave patterns, we can define a grating vector $\mathbf{K}_z$ pointing into the *z*-direction and a grating vector $\mathbf{K}_x$ pointing into the *x*-direction. The modulus of the grating vectors is given by $|\mathbf{K}_z| = 2\pi/\Lambda_z$ and $|\mathbf{K}_x| = 2\pi/\Lambda_x$, where Λ_z and Λ_x are the grating periods,

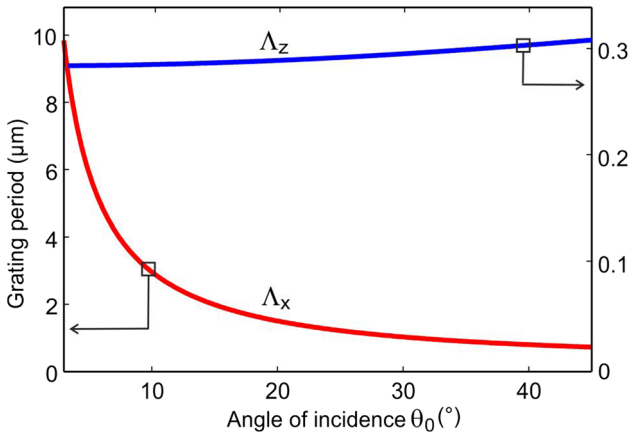

Fig. 3 Grating periods for a standing wave pattern in a V-resonator inside the disk as a function of the angle of incidence θ_0. The laser wavelength is 1030 nm, and the refractive index is 1.82

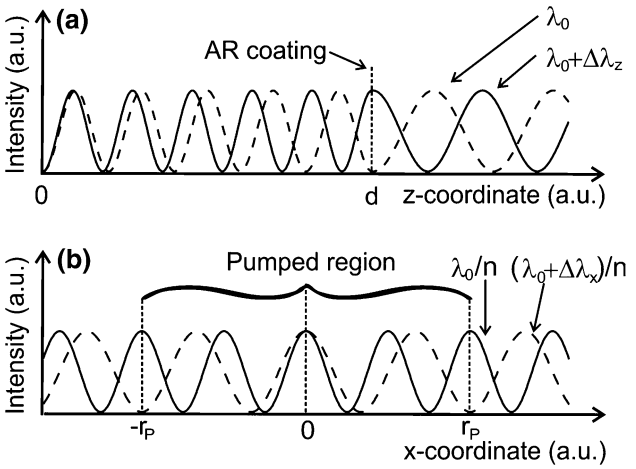

Fig. 4 Standing wave intensity patterns of a pair of adjacent longitudinal modes with the required wavelength difference for dephasing **a** in the z-direction at the AR coating of the disk and **b** in the x-direction at the edge of the pump spot; **b** shows the standing wave patterns in the x-direction for $y = 0$ and $z = \lambda_0/(2n)$

respectively. An examination of the roots of Eq. (5) yields the grating period along the x-axis

$$\Lambda_x = \frac{\lambda_0}{2n\sin\theta} = \frac{\lambda_0}{2\sin\theta_0}. \tag{7}$$

Accordingly, the grating period along the z-axis is

$$\Lambda_z = \frac{\lambda_0}{2n\cos\theta} = \frac{\lambda_0}{2\sqrt{n^2 - \sin^2\theta_0}}. \tag{8}$$

Equations (8) and (7) are plotted in Fig. 3 for a wavelength of 1030 nm. The period of the grating along the x-axis Λ_x depends strongly on the angle of incidence, while the grating period along the z-axis Λ_z depends only weakly on the angle of incidence.

Until here, we examined the standing wave pattern of one single longitudinal mode. When two or more longitudinal modes are present in the resonator, the standing wave pattern exhibits beating frequencies according to the frequency difference of the modes. Integration of this pattern over several periods of the beating frequency yields a time-averaged standing wave pattern. The time-averaged stationary standing wave pattern is equal to the sum of the individual standing wave patterns of the modes. Thus, we can sum up the stationary intensity patterns of the longitudinal modes.

2.3 Spatial dephasing of standing waves

In the introduction, we have calculated the necessary wavelength difference so that the standing wave patterns of two modes are out of phase at the AR-coated side of the disk for an I-resonator. The same can be done for a V-resonator. The required wavelength difference for dephasing of two standing wave patterns in the z-direction, $\Delta\lambda_z$, is given by

$$\Delta\lambda_z = \frac{\lambda_a^2}{4dn\cos\theta} = \frac{\lambda_a^2}{4d\sqrt{n^2 - \sin^2\theta_0}}. \tag{9}$$

The standing wave pattern in a V-resonator has a different grating period in the x-direction, as shown in Fig. 3. In this direction, the standing wave patterns of two modes can be spatially out of phase as well and exploit gain at the edge of the circular pump spot (see Fig. 4). However, numerical calculations for large angles of incidence and pump radii up to 2.75 mm have shown that there is no significant gain benefit for dephased standing wave patterns in the x-direction. The required wavelength difference for dephasing of two standing wave patterns in the x-direction, $\Delta\lambda_x$, is given by

$$\Delta\lambda_x = \frac{\lambda_a^2}{4r_p n\sin\theta} = \frac{\lambda_a^2}{4r_p\sin\theta_0}, \tag{10}$$

where r_p is the radius of the circular pump spot having a flat top pumping profile. The graph in Fig. 5 shows the necessary wavelength difference for the dephasing of two patterns as a function of the angle of incidence for an average wavelength of 1030 nm. In thin-disk lasers, the necessary wavelength difference is on the nanometer scale. The necessary wavelength difference gives a good qualitative understanding of the influence of spatial hole burning on the optical spectrum of a laser. However, for quantitative results the mode competition has to be simulated.

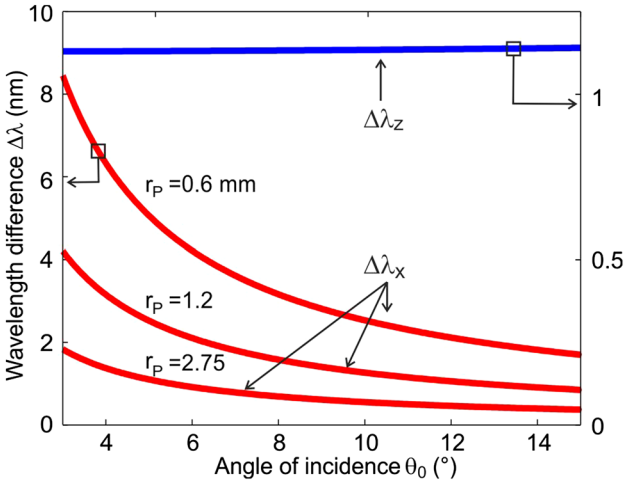

Fig. 5 The necessary wavelength differences $\Delta\lambda_x$ and $\Delta\lambda_z$ for two standing wave patterns to dephase in the x-direction and in the z -direction at the edges of the gain medium. The average wavelength is 1030 nm, the refractive index is 1.82, the thickness of the disk is 130 µm, and r_p is the radius of the circular pump spot

3 Stationary rate equation model for Yb:YAG thin-disk lasers with spatial hole burning

Optical transitions in the Yb-ion take place between two electronic states. The electronic state $^2F_{7/2}$ is the ground state, and the electronic state $^2F_{5/2}$ is the excited state. The crystal field of the YAG host lattice splits the ground state into four energy levels and the excited state into three energy levels. The energy levels of the ground state are thermally populated at room temperature, due to their small energy difference.

At a wavelength of 1030 nm, the upper laser level is the lowest energy level of the excited state and the lower laser level is the third energy level of the ground state. Since the lower laser level is thermally populated, the lasing threshold of quasi-three level lasers is made up of two independent thresholds: a transparency threshold and a resonator threshold. The transparency threshold is the threshold at which the crystal becomes transparent for the laser light. The resonator threshold is given by the loss due to output coupling and residual losses in the resonator, e.g., due to scattering.

The kinetics in Yb:YAG thin-disk lasers in single mode operation can be described by two coupled rate equations: one for the gain and one for the intensity of a particular mode. We use measured effective cross sections to describe the kinetics of the quasi-three level laser [8]. Using effective cross sections, we can define a coefficient B_m that incorporates the effective cross sections for absorption and emission at the pump wavelength and the effective cross sections for absorption and emission at the wavelength of the m-th mode [9]:

$$B_m = \frac{\sigma_{abs,P}}{\sigma_{abs,P} + \sigma_{em,P}} \frac{\sigma_{abs,m} + \sigma_{em,m}}{\sigma_{abs,m}} \tag{11}$$

where $\sigma_{abs,P}$ and $\sigma_{em,P}$ are the effective cross sections for absorption and emission at the pump wavelength, respectively. $\sigma_{abs,m}$ and $\sigma_{em,m}$ are the effective cross sections for absorption and emission of the m-th mode at the wavelength λ_m in vacuum. I_m is the standing wave pattern of the m-th mode. The intensity of the laser mode I_m and the intensity of the pump light I_P are normalized to their respective saturation intensities:

$$i_m = \frac{I_m}{I_m^{sat}} = I_m \frac{\lambda_m (\sigma_{abs,m} + \sigma_{em,m}) \tau_{10}}{hc_0} \tag{12}$$

$$i_P = \frac{I_P}{I_P^{sat}} = I_P \frac{\lambda_P (\sigma_{abs,P} + \sigma_{em,P}) \tau_{10}}{hc_0} \tag{13}$$

where τ_{10} is the lifetime of the excited state and h is Planck's constant. The small-signal gain of the m-th mode is

$$g_{0,m} = \alpha_{0,m} \frac{(B_m - 1) i_P - 1}{1 + i_P} \tag{14}$$

where $\alpha_{0,m} = \sigma_{abs,m} n_{dop}$ is the small-signal absorption coefficient for the m-th mode and n_{dop} is the dopant concentration of the crystal. The local saturated gain coefficient for the m-th mode is given by [9, 10]

$$g_m(\mathbf{r}) = (1 + i_P) \frac{g_{0,m}}{1 + i_P + \sum_{m'=1}^{M} \frac{I_{m'}(\mathbf{r})}{I_{m'}^{sat}}} \tag{15}$$

where i_P is the normalized pump intensity and M is the number of all modes. I_m is the standing wave pattern of the m-th mode. If the degeneracy of the polarization is lifted, we sum up the standing wave patterns of both polarizations in the denominator. Hence, $\sum_{m'=1}^{M} I_{m'}^{(s)}(x,z)/I_{m'}^{sat} + \sum_{m'=1}^{M} I_{m'}^{(p)}(x,z)/I_{m'}^{sat}$ replaces $\sum_{m'=1}^{M} I_{m'}(\mathbf{r})/I_{m'}^{sat}$.

Thin-disk lasers are usually pumped by a multipass pumping scheme. Due to multiple passes of the pump light through the disk, the pump intensity is assumed to be constant in the z-direction of the disk to a good approximation. Additionally, we assume that the pumped area has a circular shape with a flat top intensity profile. The flat top intensity profile is justified because in our experiment the pump spot is best approximated by a super-Gaussian of order 12. The radius of the flat top intensity profile is equal to the radius at which the fitted super-Gaussian profile has

dropped to half of its maximum intensity value. A slight variation of the flat top radius in our simulation results in a change of threshold pump power of the longitudinal modes, but the optical spectrum is not affected. In steady-state lasing operation, a few percent of the Yb-ions are in the upper state and the ground state is depleted. Hence, the absorption is reduced. Conversely, the ground state is repopulated by stimulated emission. Thus, the absorption of the pump light also depends on the intra-cavity intensity. Therefore, we use an "effective normalized pump intensity" given by [11]

$$\mathrm{i_P} = \mathrm{i_{P,D}} R_\mathrm{P} \frac{1 - \exp\left(-M_\mathrm{P}\alpha_\mathrm{P} d\right)}{\alpha_\mathrm{P} d}, \tag{16}$$

where $\mathrm{i_{P,D}}$ denotes the diode pump intensity normalized to its saturation intensity, R_P is the combined reflectivity of the multipass pump optics, and M_P is the number of pump passes through the disk.

In an I-resonator, the product $\alpha_\mathrm{P} d$ is replaced by the integral $\int_0^d \alpha_\mathrm{P}(z)\,\mathrm{dz}$, and in a V-resonator the product is replaced by the integral $\frac{4}{A_p}\int_0^d \int_0^{r_\mathrm{p}} \alpha_P(\mathbf{r})\sqrt{r_\mathrm{p}^2 - x^2}\,\mathrm{dx}\,\mathrm{dz}$, where d is the thickness of the disk and r_p is the radius of the pumped area A_p. $\alpha_\mathrm{P}(\mathbf{r})$ is the local saturated absorption coefficient for a monochromatic pump source, which is given by [9, 10]

$$\alpha_\mathrm{P}(\mathbf{r}) = \alpha_{0,\mathrm{P}} \frac{\sum_{m'=1}^{M} \left(1 - \frac{1}{B_{\mathrm{m}'}}\right) \frac{I_{\mathrm{m}'}(\mathbf{r})}{I_{\mathrm{m}'}^{\mathrm{sat}}} + 1}{1 + \mathrm{i_P} + \sum_{m'=1}^{M} \frac{I_{\mathrm{m}'}(\mathbf{r})}{I_{\mathrm{m}'}^{\mathrm{sat}}}}, \tag{17}$$

where $\alpha_{0,\mathrm{P}} = \sigma_{\mathrm{abs,P}} n_{\mathrm{dop}}$ is the small-signal absorption coefficient at the pump wavelength. Accordingly, if the degeneracy of the polarization is lifted, $\sum_{m'=1}^{M} I_{\mathrm{m}'}^{(s)}(x,z)/I_{\mathrm{m}'}^{\mathrm{sat}} + \sum_{m'=1}^{M} I_{\mathrm{m}'}^{(p)}(x,z)/I_{\mathrm{m}'}^{\mathrm{sat}}$ replaces $\sum_{m'=1}^{M} I_{\mathrm{m}'}(\mathbf{r})/I_{\mathrm{m}'}^{\mathrm{sat}}$.

4 Self-consistent simulation of the optical spectrum of a thin-disk laser

In principle, the gain–loss balance equation would have to be solved for all longitudinal modes that can experience amplification in the gain medium. Our calculations have shown that the number of modes that appear in the optical spectrum of the laser does not change as long as the spectral density of the modes that we use in the calculation is not coarser than one-tenth of the wavelength difference required for dephasing of two neighboring modes over the thickness of the disk. This means that for a 0.5-m-long resonator, we only need to include every hundredth longitudinal mode in our simulation which saves considerable computing time.

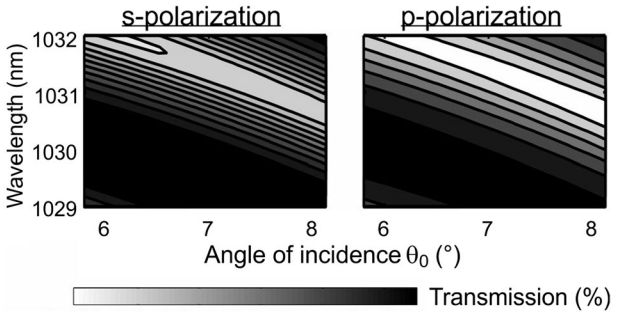

Fig. 6 Transmission of the Fabry–Pérot interferometer formed by the disk. The AR coating and the HR coating are optimized for 1030 nm. Transmitted laser light is absorbed by the heat sink. These transmission values were used in the simulations

The AR-coated front side and the HR-coated back side of the disk form a Fabry–Pérot interferometer, because of the residual reflection from the AR coating. This interferometer can shift the laser wavelengths by some tenths of a nanometer. It has a free spectral range which is exactly twice the dephasing length of the spatial hole burning along the z-direction. Thus, the spectral reflectivity of this Fabry–Pérot interferometer has to be included in the simulation. We have neither information about the AR coating nor about the HR coating. Therefore, we assume a typical HR coating that comprises 14 double layers of Ta_2O_5 and SiO_2 [6]. The thickness of the layers is chosen such that the maximum reflectivity is at 1030 nm. The peak transmission of the AR coating is assumed to be at the same wavelength. The AR coating is assumed to comprise of a layer of MgF_2, followed by a layer of SiO_2. The transmission of the disk with the AR coating on its front side and the HR coating on its back side is shown in Fig. 6. The HR coating does not affect the simulated optical spectrum if the coating is comprised of at least eight double layers. Only the threshold pump power of the longitudinal modes is slightly decreasing if there are more than eight double layers. Conversely, the AR coating can alter the simulated optical spectrum. As the laser beam is transmitted twice as often by the AR coating as it is reflected by the HR coating. Additionally, the AR coating is optimized for 1030 nm and the transmission changes about 0.1 % between 1029.5 and 1030.5 nm. In the case of the I-resonator for instance, the wavelength of the modes can be shifted by approximately 0.1 nm in the simulations, depending on the optimized wavelength.

Values used in the simulations are shown in Table 1. The loss factor R_P due to multiple reflections of the pump light at the parabolic mirror and at the prisms was chosen such that our simulation yields the measured output power. At the beginning of the simulation, we distribute power over the examined modes according to the absorbed pump power and to the fluorescence spectrum of Yb:YAG. Then

Table 1 Values used in the simulation. We assume monochromatic pumping, but the pump wavelength depends on the diode pump power P_D. This dependence has been measured for our laser

Parameter	Description	Value
λ_P (P_D)	Pump wavelength	930–941 nm
M_P	Pump passes	32
d	Thickness of the disk	130 µm
n_dop	Dopant concentration	9 at.%
L_res	Losses in the resonator	$8 \cdot 10^{-4}$
r_p	Pump spot radius	2.75 mm
$\bar{T}_\mathrm{D}$	Mean disk temperature	Eq. (24)
$T_\mathrm{OC}(\lambda)$	Output coupling	from datasheet
R_P	Pump loss factor	0.77
R_1	HR mirror reflectivity	0.9998

we iterate the gain–loss balance equation until the change of power of each mode is below a certain threshold. The threshold depends on whether an I-resonator or a V-resonator is simulated.

4.1 I-resonator

The gain–loss balance equation of the m-th mode for an I-resonator is given by [12]

$$\int_0^d \frac{I_\mathrm{m}(z)/I_{0,}m \,\mathrm{dz}}{1 + \mathrm{i_P} + \sum_{m'=1}^{M} I_{\mathrm{m}'}(z)/I_{\mathrm{m}'}^\mathrm{sat}} = \gamma_\mathrm{loss}^{(I)}, \tag{18}$$

where $\gamma_\mathrm{loss}^{(I)}$ is the round-trip loss coefficient for an I-resonator, $I_\mathrm{m}(z) = I_{0,}m \sin^2(k_\mathrm{m} z)$ is the standing wave pattern of the m-th mode in an I-resonator, and $I_{0,}m$ is the maximum intensity of this pattern. The round-trip loss coefficient $\gamma_\mathrm{loss}^{(I)}$ is defined by

$$\gamma_\mathrm{loss}^{(I)} := -\ln R_\mathrm{D}\left(1 - T_\mathrm{OC}\right) - \ln\left(1 - L_\mathrm{res}\right), \tag{19}$$

where T_OC is the output coupler transmission and R_D is the reflectivity of the Fabry–Pérot interferometer. L_res accounts for residual losses e.g., due to scattering etc. during one round trip in the resonator.

The intensity of a mode is then calculated by iteratively solving

$$I_\mathrm{m}^{(n)} = I_\mathrm{m}^{(n-1)} \times \exp\left[\int_0^d \frac{I_\mathrm{m}(z)/I_{0,}m}{1 + \mathrm{i_P} + \sum_{m'=1}^{M} I_{\mathrm{m}'}(z)/I_{\mathrm{m}'}^\mathrm{sat}} \,\mathrm{dz} - \gamma_\mathrm{loss}^{(I)}\right], \tag{20}$$

where $I_\mathrm{m}^{(n-1)}$ is the intensity of the m-th mode of the previous iteration and $I_\mathrm{m}^{(n)}$ is the intensity of the m-th mode in the current iteration. The iteration stops when the relative change of power of each mode is smaller than 10^{-6}.

4.2 V-resonator

The gain–loss balance equation of the m-th mode for a V-resonator and for the s-polarization reads

$$\frac{4}{A_p}\int_0^d\int_0^{r_\mathrm{p}} \frac{I_\mathrm{m}^{(s)}(x,z)}{I_{0,m}^{(s)}} g_\mathrm{m}(x,z)\sqrt{r_\mathrm{p}^2 - x^2}\,\mathrm{dx}\,\mathrm{dz} = \gamma_\mathrm{loss}^{(V)}, \tag{21}$$

where $\gamma_\mathrm{loss}^{(V)}$ is round-trip loss coefficient for a V-resonator and $I_\mathrm{m}^{(s)}(x,z)$ is the s-polarized standing wave pattern of the m-th mode. $I_{0,m}^{(s)}$ is the maximum intensity of the s-polarized m-th mode. The pumped area of the disk is $A_p = \pi r_\mathrm{p}^2$. $\gamma_\mathrm{loss}^{(V)}$ is defined by

$$\gamma_\mathrm{loss}^{(V)} := -\ln R_1 R_\mathrm{D}^2\left(1 - T_\mathrm{OC}\right) - \ln\left(1 - L_\mathrm{res}\right), \tag{22}$$

where R_1 is the reflectivity of the HR mirror. The intensity of each mode is then calculated by iteratively applying

$$I_\mathrm{m}^{(n)} = I_\mathrm{m}^{(n-1)} \times \exp\left[\frac{4}{A_p}\int_0^d\int_0^{r_\mathrm{p}} \frac{I_\mathrm{m}^{(p)}}{I_{0,m}^{(p)}} g_\mathrm{m}\sqrt{r_\mathrm{p}^2 - x^2}\,\mathrm{dx}\,\mathrm{dz} - \gamma_\mathrm{loss}^{(V)}\right]. \tag{23}$$

The intensity of a p-polarized mode is calculated accordingly. The iteration stops when the relative change of power of each mode is smaller than 10^{-4}.

5 Comparison of experimental results and numerical investigations

5.1 Experimental setup and simulation

The laser consists of a thin-disk laser head and a 16-pass pump cavity manufactured by Trumpf GmbH & Co. KG. The thin-disk laser was pumped by diode bars at a wavelength of 940 nm. The optical spectrum of the laser was measured with an optical spectrum analyzer (HP 71450B), having a spectral resolution of 0.1 nm. For a spectral range from 1029 nm to 1032 nm, the sweep time was approximately 300 ms. The optical spectra were averaged over 30 measurements, in order to cancel fluctuations during the measurement. In the measured optical spectrum, a laser mode appears to have a linewidth of several tenths

of a nanometer, so we are just measuring the instrument function. Our simulation is using modes with a spacing of 0.01 nm, which is much smaller than the resolution of 0.1 nm of our spectrum analyzer. Therefore, the spacing of the modes in the simulation is well below the maximum allowed spacing of approximately 0.1 nm (see Sect. 4.1). For better comparison between the simulated optical spectra and the measured optical spectra, the simulated ones are artificially broadened by folding them with the transfer function of the optical spectrum analyzer.

The absorption cross sections and emission cross sections of Yb:YAG are temperature dependent. For this reason, we used an IR-camera (FLIR ThermaCam E25) to measure the temperature profile of the thin-disk's surface. Since the emissivity of the AR-coated front side of the Yb:YAG disk is unknown, we calibrated the temperature measurement by pumping water from a heated reservoir through the disk. In a next step, we measured the surface temperature of the disk when the disk was pumped by diode lasers. Then we averaged the temperature over the pumped area of the disk. Assuming one-dimensional heat flow, we derived an approximate formula describing the mean disk temperature as a function of the diode pump power P_D:

$$\bar{T}_\mathrm{D}(P_\mathrm{D}) = 1.42\frac{K}{W^2}\cdot P_\mathrm{D}^2 - 2.64\cdot 10^{-3}\frac{K}{W}\cdot P_\mathrm{D} + 300\,\mathrm{K}. \tag{24}$$

5.2 I-resonator

We measured the optical spectrum of an Yb:YAG thin-disk laser having an I-resonator as a function of the pump power for output coupler transmissions of 2 and 4.5 %. Figure 7a shows the experimental setup, consisting of the thin disk, an outcoupling mirror, and the pump optics. The measured spectra are shown in Fig. 8a and c, and the corresponding simulated spectra are shown in Fig. 8b and d. For each diode pump power, the spectra have been normalized to their maximum value. The wavelengths of the peak intensities of the measured spectra and the simulated spectra exhibit only a small systematic difference; the peak intensities in the simulated spectra are shifted by approximately 0.4 nm toward longer wavelengths in comparison with the measured spectra.

Both the measured and the simulated spectra show a single peak at low pumping powers and two peaks at high pumping powers. The reason for this transition from a single peak to two peaks is that the laser prefers a combination of modes that facilitates the highest saturation of the gain. The number of peaks in the measured spectra agrees with the number of peaks in the simulated spectra. The pumping powers where the spectrum splits into two branches are identical in the simulation and the measurement. This indicates that our simulation models the laser system accurately. The distance between the dashed lines in Fig. 8 represents the wavelength difference $\Delta\lambda$ that is necessary for the dephasing of two standing wave patterns, see Sect. 1. These wavelength differences $\Delta\lambda$ fit well to the measured spectra and the simulated spectra.

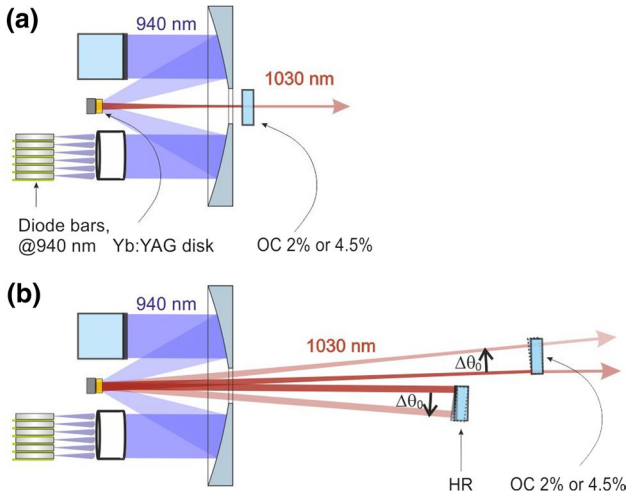

Fig. 7 Experimental setups for the measurement of the optical spectrum of the thin-disk laser; **a** the shortest possible setup of an I-resonator. **b** a V-resonator where the angle of incidence is gradually changed from 5.8° to 8.2°

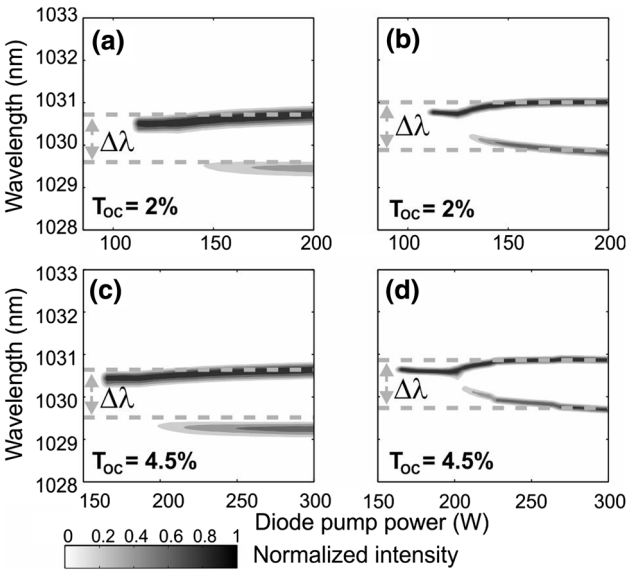

Fig. 8 **a** and **c** shows measured optical spectra as a function of the diode pump power for output coupler transmissions of 2 and 4.5 %, respectively; **b** and **d** shows the result of the simulation for these output coupler transmissions. The *dashed lines* denote the necessary wavelength difference for dephasing over a distance of one disk thickness

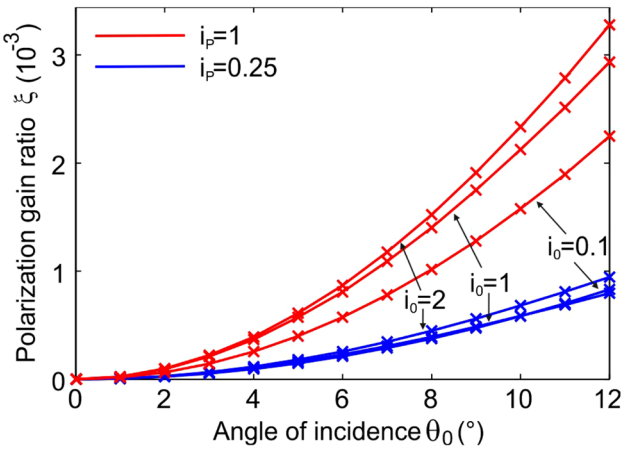

Fig. 9 Numerical solution of the gain ratio of *p*-polarization to *s* -polarization in the case of one *p*-polarized mode and one *s*-polarized mode having an intensity of $i_0/2$, respectively. The thickness of the disk is 130 µm, the radius of the pumped area is 2.75 mm, and the wavelength is 1030 nm

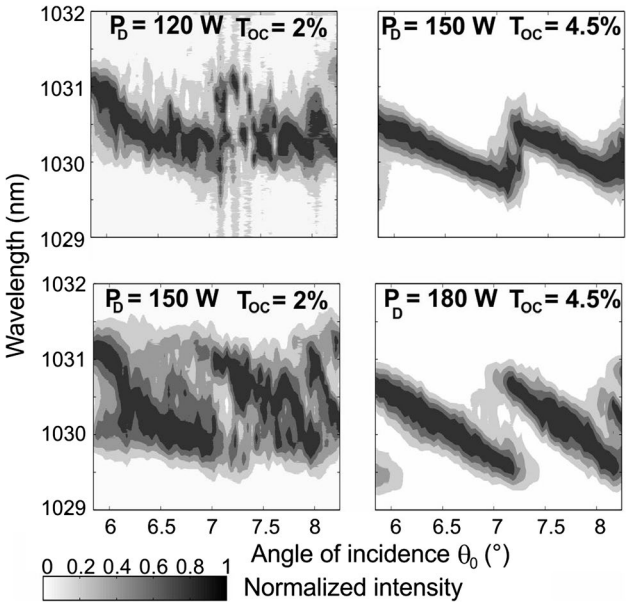

Fig. 10 Measured optical spectra as a function of the angle of incidence for three pump powers and two output coupler transmissions. For each angle of incidence, the optical spectrum was normalized to its maximum value

5.3 V-resonator

5.3.1 Polarization-dependent gain

As mentioned in Sect. 2.2, the *p*-polarized standing wave pattern can exploit gain that cannot be exploited by the *s* -polarized standing wave pattern. This gives rise to the question whether the laser output is polarized. Therefore, we determine the gain ratio when a *p*-polarized mode and a *s*-polarized mode with equal intensities and wavelengths of 1030 nm are present in the resonator. The gain ratio of the *p*-polarized mode to the *s*-polarized mode as a function of the angle of incidence θ_0 is then given by

$$\xi(\theta_0) = \frac{\int_0^d \int_0^{r_\mathrm{p}} \frac{I^{(p)}/I_0^{(p)}}{1+i_\mathrm{P}+i_0\left(I^{(s)}/I_0^{(s)}+I^{(p)}/I_0^{(p)}\right)} \sqrt{r_\mathrm{p}^2-x^2}\,\mathrm{d}x\,\mathrm{d}z}{\int_0^d \int_0^{r_\mathrm{p}} \frac{I^{(s)}/I_0^{(s)}}{1+i_\mathrm{P}+i_0\left(I^{(s)}/I_0^{(s)}+I^{(p)}/I_0^{(p)}\right)} \sqrt{r_\mathrm{p}^2-x^2}\,\mathrm{d}x\,\mathrm{d}z}. \quad (25)$$

Equation (25) is solved by numerical integration. Figure 9 depicts its numerical solution. The gain ratio $\xi(\theta_0)$ shows a slight advantage for the *p*-polarization. The larger the angle of incidence, the higher is the gain advantage for the *p*-polarization. However, in our experiments we never observed polarized emission, even for angles of incidence of 15°.

5.3.2 Gradually changing the angle of incidence

We measured the influence of the angle of incidence on the optical spectrum of the laser with the setup shown in Fig. 7b). The angle of incidence was gradually increased by increasing the tilting angle of the HR mirror. Then we realigned the output coupler until the output power reached its maximum value. The angle of incidence was increased from 5.8° to 8.2° in steps of 0.04°. The optical spectra were measured for two output coupler transmissions of 2 and 4.5 % and three diode pump powers. The results are shown in Fig. 10. When using an output coupler transmission of 2 %, the optical spectra have a spectral width of approximately 1.1 nm and one cannot clearly identify individual peaks in the optical spectrum.

With an output coupler transmission of 4.5 %, the peak wavelength decreases monotonically as the angle of incidence increases from 5.8° to 7.1°. At an angle of incidence of 7.1°, the peak wavelength jumps to a longer wavelength. We suppose that this is the influence of the Fabry–Pérot interferometer, which is formed by the AR-coated front side and the HR-coated back side of the disk. The spectral reflectivity of the etalon has a strong influence on the optical spectrum of the laser for the measured pump powers, because the intra-cavity intensity is not much higher than the saturation intensity for the pump powers used in the experiments.

We simulated the influence of the angle of incidence on the optical spectrum for an output coupler transmission of 4.5 % and a diode pump power of 150 W. The simulation employed the coating design described in Sect. 4. In the simulation, the standing wave patterns were sampled with at least two sampling points per grating period Λ_x, which is the minimum sampling according to the Nyquist theorem. The results are shown in Fig. 11. The simulation yields two

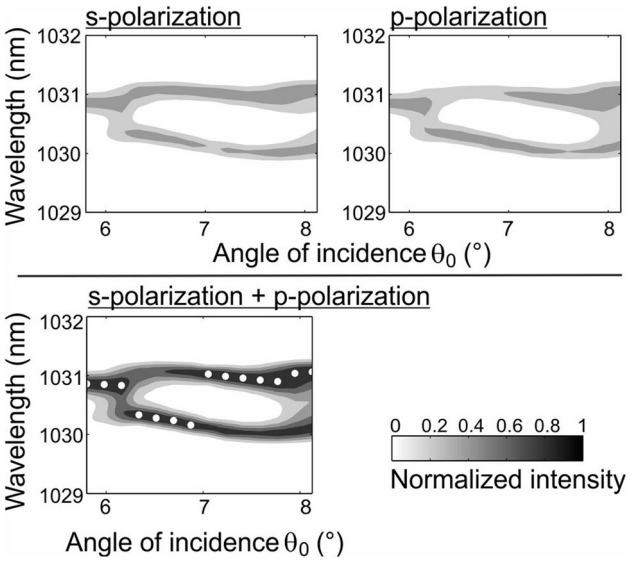

Fig. 11 Simulation of the optical spectrum as a function of the angle of incidence for a diode pump power of 150 W and an outcoupling of 4.5 %. The *s*-polarized intensity, the *p*-polarized intensity, and the sum are shown. In the sum, the wavelengths of the highest intensity are marked with *white dots*. The intensities have been normalized to the maximum of the summed intensity for each angle of incidence

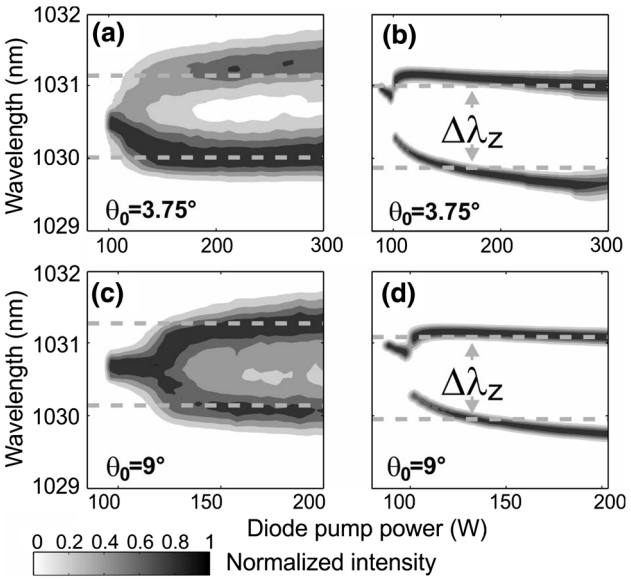

Fig. 12 **a** and **c** depicts measured optical spectra for two different angles of incidence; **b** and **d** shows the results of the simulation. The output coupler transmission was 2 %. The intensities have been normalized to their maximum for each diode pump power. The *dashed lines* denote the necessary wavelength difference for dephasing in the *z*-direction over a distance of one disk thickness

optical spectra: one for the *s*-polarization and one for the *p*-polarization. As shown in Sect. 5.3.1, the *p*-polarization has a slight gain advantage in comparison with the *s*-polarization. However, the simulated optical spectra exhibit nearly equal spectral intensities for the *s*-polarization and for the *p*-polarization. We attribute this to the higher reflectivity of the coating on the disk for the *s*-polarization. Although the simulated optical spectrum shows emission at two distinct wavelengths, it can be seen that the wavelength of the highest intensity which is indicated by white dots in Fig. 11, monotonically decreases as the angle of incidence increases from 5.8° to 7°. Then this wavelength jumps to a higher value, as observed in the experiment. When the spectral reflectivity of the Fabry–Pérot interferometer was neglected, the angle of incidence had no influence on the optical spectrum in the simulation.

5.3.3 Optical spectrum as a function of the pump power

The measured optical spectrum as a function of the diode pump power for an output coupler transmission of 2 % and angles of incidence of 3.75° and 9° are shown in Fig. 12. The simulated spectra are shown for comparison on the right of Fig. 12. They have been simulated by spatially averaging over the *x*-direction. Thus, the dependence on the *x*-axis vanishes and the simulation converges roughly two orders of magnitudes faster. Although the wavelengths occurring in the optical spectrum for pump powers higher than 150 W are in good agreement with the experiments, the spectral intensity of the branches is not. However, the distance between the branches roughly fits to the necessary wavelength difference for dephasing of two standing wave patterns over a distance of one disk thickness. The required wavelength difference in the *z*-direction according to Sect. 2.2 is shown in the figure by the dashed lines.

6 Conclusion

Spatial hole burning is responsible for the overall shape of the optical spectrum of a thin-disk laser, because it determines the number of longitudinal modes. For V-resonators, the Fabry–Pérot interferometer that is formed by residual reflection from the AR-coated front side and reflection from the HR-coated back side of the disk also has a strong influence on the output spectrum. Our measurements and simulations have shown that the optical spectrum of the laser depends on the angle of incidence on the disk. At pump levels below the threshold for longitudinal multimode operation, it is even possible to tune the laser wavelength by 1 nm by changing the angle of incidence. The gain advantage for the *p*-polarization is <0.1 % for angles of incidence smaller than 5° and <0.3 % for angles of incidence smaller than 12°, assuming that the pump intensity and the intra-cavity intensity are equal to their respective saturation intensities. The simulations show that the gain

advantage for *p*-polarization is partially compensated by a higher reflectivity for the *s*-polarization of the etalon that is formed by the AR coating on the front side and the HR coating on the back side of disk. In the experiments, no polarized laser output was observed.

In the I-resonator, the threshold for multimode operation and the number of longitudinal modes in the simulated optical spectral are in good agreement with the measured optical spectra. We did not implement any kind of energy migration in the Yb:YAG crystal in the simulation; due to the good agreement between measurement and simulation, we assume that energy migration plays only a minor role for dopant concentrations less than or equal to 9 at.%.

Finally, the presented simulation of the mode competition allows to evaluate intra-cavity spectral filters numerically. Further studies should measure the optical spectrum with higher spectral and temporal resolution.

Acknowledgments We gratefully acknowledge the support of the Deutsche Forschungsgemeinschaft under reference number WI 1939/4-1 and of Trumpf GmbH & Co. KG.

References

1. S. Ricaud, A. Jaffres, P. Loiseau, B. Viana, B. Weichelt, M. Abdou-Ahmed, A. Voss, T. Graf, D. Rytz, M. Delaigue, E. Mottay, P. Georges, F. Druon, Opt. Lett. **36**(21), 4134 (2011)
2. B. Braun, K.J. Weingarten, F.X. Kärtner, U. Keller, Appl. Phys. B **61**, 429 (1995). doi:10.1007/BF01081271
3. F. Kärtner, B. Braun, U. Keller, Appl. Phys. B **61**(6), 569 (1995)
4. C. Vorholt, U. Wittrock, in Lasers and Electro-Optics Europe (CLEO EUROPE/IQEC), 2013 Conference on and International Quantum Electronics Conference, pp. 1–1 (2013)
5. R. Paschotta, J. Aus der Au, G. Spühler, S. Erhard, A. Giesen, U. Keller, Appl. Phys. B **72**(3), 267 (2001)
6. S. Günster, D. Ristau, B. Weichelt, A. Voss, in Society of Photo-Optical Instrumentation Engineers (SPIE) Conference Series, vol. 8168 (SPIE), vol. 8168, p.40 (2011)
7. P. Yeh, *Optical Waves in Layered Media. Wiley Series in Pure and Applied Optics*, 2nd edn. (Wiley, NewYork, 2005)
8. J. Körner, C. Vorholt, H. Liebetrau, M. Kahle, D. Kloepfel, R. Seifert, J. Hein, M.C. Kaluza, J. Opt. Soc. Am. B **29**(9), 2493 (2012)
9. S. Bowman, S. O'Connor, S. Biswal, N. Condon, A. Rosenberg, IEEE J. Quantum Electron. **46**(7), 1076 (2010)
10. Y. Sato, T. Taira, IEEE J. Quantum Electron. **40**(3), 270 (2004)
11. K. Contag, M. Karszewski, C. Stewen, A. Giesen, H. Hugel, Quantum Electron. **29**(8), 697 (1999)
12. J.J. Zayhowski, Opt. Lett. **15**(8), 431 (1990)